or gender; however, the Alzheimer's disease group was significantly less educated than the healthy control group. As expected, significant differences between the two groups were observed for CDR and CDR-SOB scores, cognitive performance (MMSE, episodic memory, and non-memory scores), and brain volumetrics (grey matter and hippocampal volumes).

No toxic event was observed in the current clinical PET study. After intravenous administration of $^{18}$F-THK5105, all subjects showed rapid entry of the tracer into grey matter areas. The SUV time activity curves of $^{18}$F-THK5105 PET are shown in Fig. 2. The peak uptake and clearance rates of $^{18}$F-THK5105 in the cerebellar cortex were similar between healthy control (Fig. 2A) and Alzheimer's disease (Fig. 2B) groups. In patients with Alzheimer's disease, the inferior temporal cortex, which is an area known to contain high densities of neurofibrillary tangles in Alzheimer's disease (Bouras *et al.*, 1994), showed $^{18}$F-THK5105 retention compared to the cerebellum, especially at the later time points. In contrast, time activity curves in the inferior temporal cortex of healthy control subjects were nearly identical to those in the cerebellum. The subcortical white matter region showed relatively lower entry and slower clearance than grey matter areas, but no significant differences were observed for time activity curves between healthy control and Alzheimer's disease groups (data not shown). The ratio of inferior temporal cortex to cerebellar SUVR became constant in all participants ~90 min after injection of $^{18}$F-THK5105 (Fig. 2C). Therefore, we selected SUVR values from 90–100 min post-injection for the following analysis.

Summed SUVR images from 90–100 min post-injection for healthy control and Alzheimer's disease subjects are shown in Fig. 3. Contrasted with a lack of remarkable $^{18}$F-THK5105 retention in the grey matter of healthy control subjects, patients with Alzheimer's disease showed high grey matter $^{18}$F-THK5105 retention in the lateral and mesial temporal regions. $^{18}$F-THK5105 retention was additionally observed in the brain stem; however, similar retention in these areas was detected in healthy control subjects. When comparing the 90–100 min regional SUVR in Alzheimer's disease and healthy control subjects, $^{18}$F-THK5105 SUVRs for the ventrolateral prefrontal, medial orbitofrontal, superior, and inferior temporal, parietal, posterior cingulate, and mesial temporal cortices were significantly higher in patients with Alzheimer's disease (Table 2 and Fig. 4). Notably, SUVR in the inferior temporal cortex showed no overlap between the Alzheimer's disease and healthy control groups (Fig. 4). $^{18}$F-THK5105 retention in other neocortical areas was relatively lower than in the inferior temporal area. The SUVR in the parietal cortex was elevated in 62.5% (5/8) of patients with Alzheimer's disease; however, $^{18}$F-THK5105 retention in the ventrolateral prefrontal cortex was only elevated in 37.5% (3/8) of patients with Alzheimer's disease. Mesial temporal $^{18}$F-THK5105 retention was significantly higher in patients with Alzheimer's disease than in healthy control subjects. However, a substantial overlap of SUVR was observed between both groups. The SUVR values in the pons and subcortical white matter were nearly identical in both groups, but higher than other neocortical regions. The effect size value between Alzheimer's disease and healthy control subjects was highest in the inferior temporal cortex, followed by the superior temporal, posterior cingulate, parietal, and medial orbitofrontal cortices and was lowest in the other regions examined (Table 2). Regional difference of $^{18}$F-THK5105 retention was additionally examined in healthy control subjects. As a result, mesial temporal $^{18}$F-THK5105 retention (mean SUVR = 1.17) was significantly higher than neocortical $^{18}$F-THK5105 retention (mean SUVR = 1.05) in healthy control subjects.

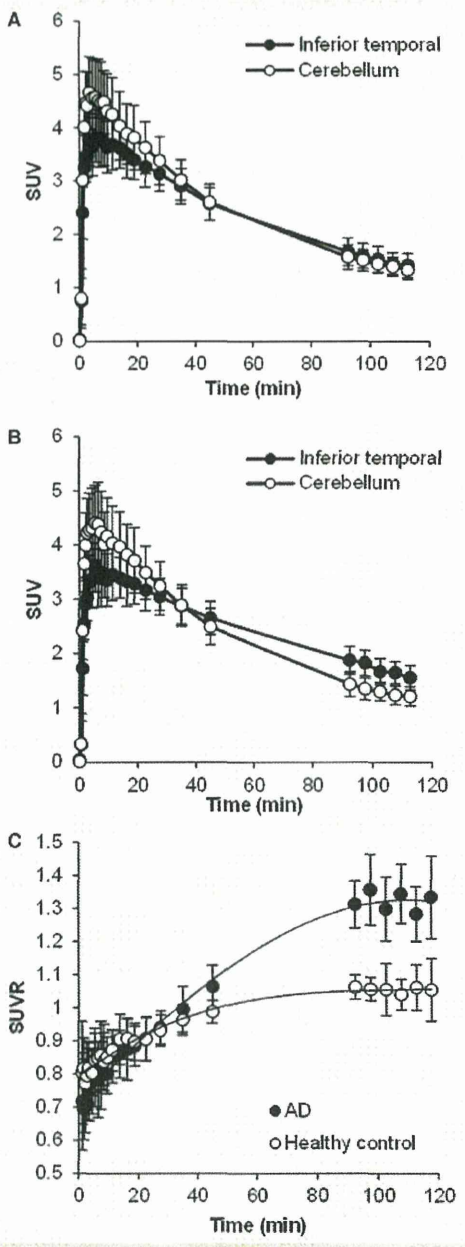


**Figure 2** (**A** and **B**) $^{18}$F-THK5105 SUV TACs in the cerebellum (open circles) and inferior temporal cortex (filled circles) of eight healthy control subjects (**A**) and eight patients with Alzheimer's disease (**B**). (**C**) SUVR time activity curves of $^{18}$F-THK5105 PET in eight healthy control subjects (open circles) and eight patients with Alzheimer's disease (AD) (filled circles). Each point represents the mean ± SD.

As reported in previous PET studies (Klunk *et al.*, 2004; Mintun *et al.*, 2006; Rowe *et al.*, 2007), $^{11}$C-PiB SUVR values were significantly greater in the neocortical regions of patients with Alzheimer's disease compared to healthy control subjects (Table 3). All patients with Alzheimer's disease showed marked and extensive PiB retention in neocortical areas. On the other hand, neocortical PiB retention in healthy control subjects was not significant, except for one healthy control case that only showed high $^{11}$C-PiB retention in the frontal cortex. In contrast

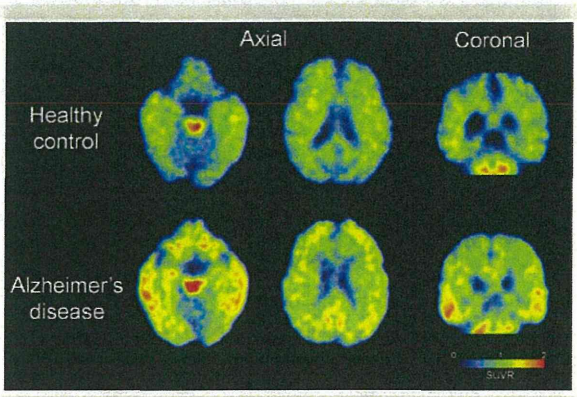


**Figure 3** $^{18}$F-THK5105 PET images from 60–80 min post-injection in a healthy control subject (72-years-old, CDR 0, MMSE 29) and a patient with Alzheimer's disease (68-years-old, CDR 1.0, MMSE 20).

**Table 2 Regional $^{18}$F-THK5105 SUVR values in healthy control and Alzheimer's disease subjects**

| Region | Healthy controls | Alzheimer's disease | Cohen's d |
|---|---|---|---|
| Ventrolateral prefrontal | 1.08 ± 0.08 | 1.23 ± 0.14* | 1.33 |
| Lateral orbitofrontal | 1.01 ± 0.08 | 1.15 ± 0.13 | 1.32 |
| Medial orbitofrontal | 1.17 ± 0.06 | 1.29 ± 0.09* | 1.55 |
| Superior temporal | 1.04 ± 0.06 | 1.22 ± 0.07* | 2.75 |
| Inferior temporal | 1.09 ± 0.04 | 1.32 ± 0.08* | 3.58 |
| Parietal | 0.99 ± 0.08 | 1.16 ± 0.13* | 1.59 |
| Lateral occipital | 1.07 ± 0.06 | 1.18 ± 0.15 | 1.01 |
| Anterior cingulate | 1.07 ± 0.11 | 1.12 ± 0.13 | 0.35 |
| Posterior cingulate | 1.04 ± 0.08 | 1.20 ± 0.12* | 1.61 |
| Mesial temporal | 1.17 ± 0.05 | 1.26 ± 0.10* | 1.17 |
| Putamen | 1.41 ± 0.10 | 1.52 ± 0.17 | 0.83 |
| Pons | 1.88 ± 0.14 | 1.89 ± 0.23 | 0.03 |
| Subcortical white matter | 1.22 ± 0.15 | 1.22 ± 0.15 | 0.01 |
| Neocortex | 1.05 ± 0.05 | 1.23 ± 0.08* | 2.68 |

*$P < 0.05$ by the Mann–Whitney U test.

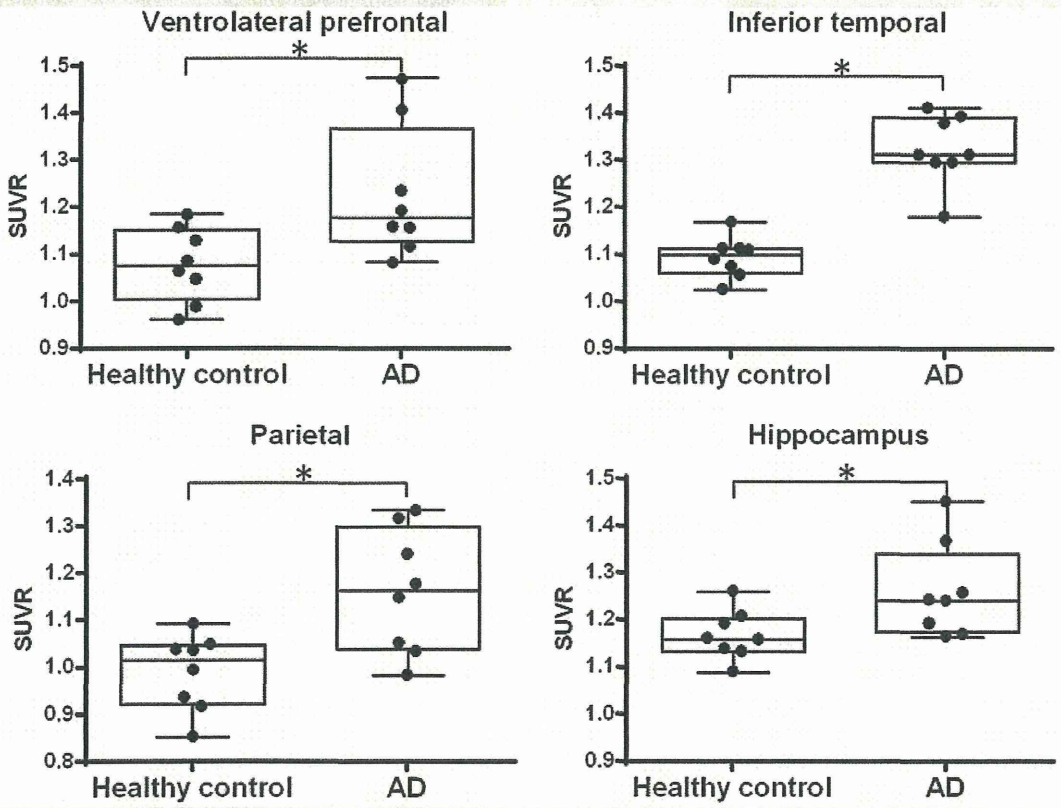


**Figure 4** Regional $^{18}$F-THK5105 SUVR values from 60–80 min post-injection in healthy control and Alzheimer's disease (AD) subjects. *$P < 0.05$ by the Mann–Whitney U test.

**Table 3 Regional $^{11}$C-PiB SUVR values in healthy control and Alzheimer's disease subjects**

| Region | Healthy controls | Alzheimer's disease | Cohen's d |
|---|---|---|---|
| Ventrolateral prefrontal | 1.32 ± 0.39 | 2.92 ± 0.82* | 2.49 |
| Lateral orbitofrontal | 1.08 ± 0.25 | 1.66 ± 0.50* | 1.46 |
| Medial orbitofrontal | 1.36 ± 0.23 | 2.38 ± 0.63* | 2.15 |
| Superior temporal | 1.11 ± 0.13 | 2.67 ± 0.67* | 3.22 |
| Inferior temporal | 1.08 ± 0.08 | 2.42 ± 0.66* | 2.88 |
| Parietal | 1.22 ± 0.17 | 2.56 ± 0.51* | 3.54 |
| Lateral occipital | 1.25 ± 0.11 | 2.07 ± 0.61* | 1.86 |
| Anterior cingulate | 1.39 ± 0.28 | 2.79 ± 0.70* | 2.64 |
| Posterior cingulate | 1.31 ± 0.24 | 3.15 ± 0.78* | 3.22 |
| Mesial temporal | 1.29 ± 0.15 | 1.65 ± 0.32* | 1.42 |
| Putamen | 1.48 ± 0.20 | 2.64 ± 0.62* | 2.50 |
| Pons | 2.04 ± 0.33 | 2.04 ± 0.40 | 0.00 |
| Subcortical white matter | 2.02 ± 0.38 | 2.06 ± 0.66 | 0.07 |
| Neocortex | 1.21 ± 0.14 | 2.75 ± 0.66* | 3.21 |

*$P < 0.05$ by the Mann–Whitney U test.

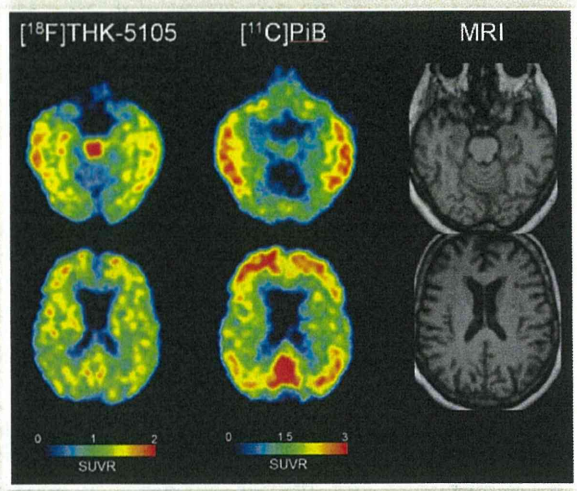


**Figure 5** $^{18}$F-THK5105 PET images from 60–80 min post-injection and $^{11}$C-PiB PET images from 40–70 min post-injection in an Alzheimer's disease patient (68-years-old, CDR 1.0, MMSE 20). Co-registered magnetic resonance images are shown on the right.

with the highest neocortical $^{18}$F-THK5105 retention in the inferior temporal cortex of patients with Alzheimer's disease, $^{11}$C-PiB retention in the same group was highest in the posterior cingulate cortex, followed by the ventrolateral prefrontal, anterior cingulate, and superior temporal cortices. The PiB effect size value between Alzheimer's disease and healthy control subjects was also highest in the parietal cortex, followed by the posterior cingulate and superior temporal cortices. As shown in Fig. 5, the pattern of cortical $^{18}$F-THK5105 retention was completely different from that of $^{11}$C-PiB retention in patients with Alzheimer's disease, which was prominent in the frontal cortex and precuneus, but not evident in the mesial temporal cortex. In contrast, $^{18}$F-THK5105 retention was evident in both lateral and mesial temporal areas but not so remarkable in other neocortical areas. There was no correlation between neocortical $^{18}$F-THK5105 and $^{11}$C-PiB SUVR values in patients with Alzheimer's disease ($r = 0.17$, $P = 0.703$). In addition, one healthy control case showing elevated PiB retention in the frontal cortex did not show any significant retention of $^{18}$F-THK5105.

Finally, we explored the relationship of neocortical or mesial temporal radiotracer retention to cognitive parameters in patients with Alzheimer's disease. Neocortical $^{18}$F-THK5105 retention was significantly correlated with MMSE scores ($r = -0.781$, $P = 0.022$), CDR ($r = 0.730$, $P = 0.050$) and CDR-SOB ($r = 0.779$, $P = 0.030$), but not correlated with composite episodic memory and non-memory scores. In contrast, neocortical $^{11}$C-PiB retention showed no significant correlation with any cognitive parameters (Fig. 6). There was no correlation between radiotracer retention in mesial temporal cortex and cognitive parameters. Furthermore, we explored the relationship of radiotracer retention with brain volumetrics. When all subjects were included in the analysis, a significant correlation was observed between mesial temporal $^{18}$F-THK5105 retention and hippocampal volumes ($r = -0.565$, $P = 0.023$) and between neocortical $^{18}$F-THK5105 retention and whole brain grey matter volumes ($r = -0.649$, $P = 0.007$). When only patients with Alzheimer's disease were included in this analysis, hippocampal volumes were significantly correlated with neocortical $^{18}$F-THK5105 retention ($r = -0.765$, $P = 0.027$), but not correlated with mesial temporal $^{18}$F-THK5105 retention. However, there were no correlations between mesial temporal $^{11}$C-PiB retention and hippocampal volumes and between neocortical $^{11}$C-PiB retention and whole brain grey matter volumes (Fig. 7).

# Discussion

In this study, the novel radiotracer $^{18}$F-THK5105 successfully differentiated patients with Alzheimer's disease from healthy control subjects. The pattern of $^{18}$F-THK5105 distribution in patients with Alzheimer's disease appears similar to the reported neurofibrillary tangle distribution in the post-mortem Alzheimer's disease brain. $^{18}$F-THK5105 retention in the inferior temporal cortex, where neurofibrillary tangle accumulation is highest in Alzheimer's disease, was observed in most patients with Alzheimer's disease. In contrast to the high frequency of $^{18}$F-THK5105 retention in the temporal cortices of Alzheimer's disease cases, ventrolateral prefrontal $^{18}$F-THK5105 retention was less frequent (3/8) and was only observed in cases with moderate-to-severe Alzheimer's disease (MMSE range 10–17). This finding is consistent with neurofibrillary tangle distribution in post-mortem Alzheimer's disease brain, where there is a higher frequency of neurofibrillary tangles in the temporal cortex than the frontal cortex (Arnold *et al.*, 1991; Bouras *et al.*, 1994; Haroutunian *et al.*, 1999). It is also in agreement with recent PET results using other novel radiotracers ($^{18}$F-T807 and $^{18}$F-T808) that demonstrated higher radiotracer retention in the lateral temporal lobe compared to the frontal lobe and selective binding ability to paired helical filament tau (Chien *et al.*, 2013, 2014). These findings suggest a spreading

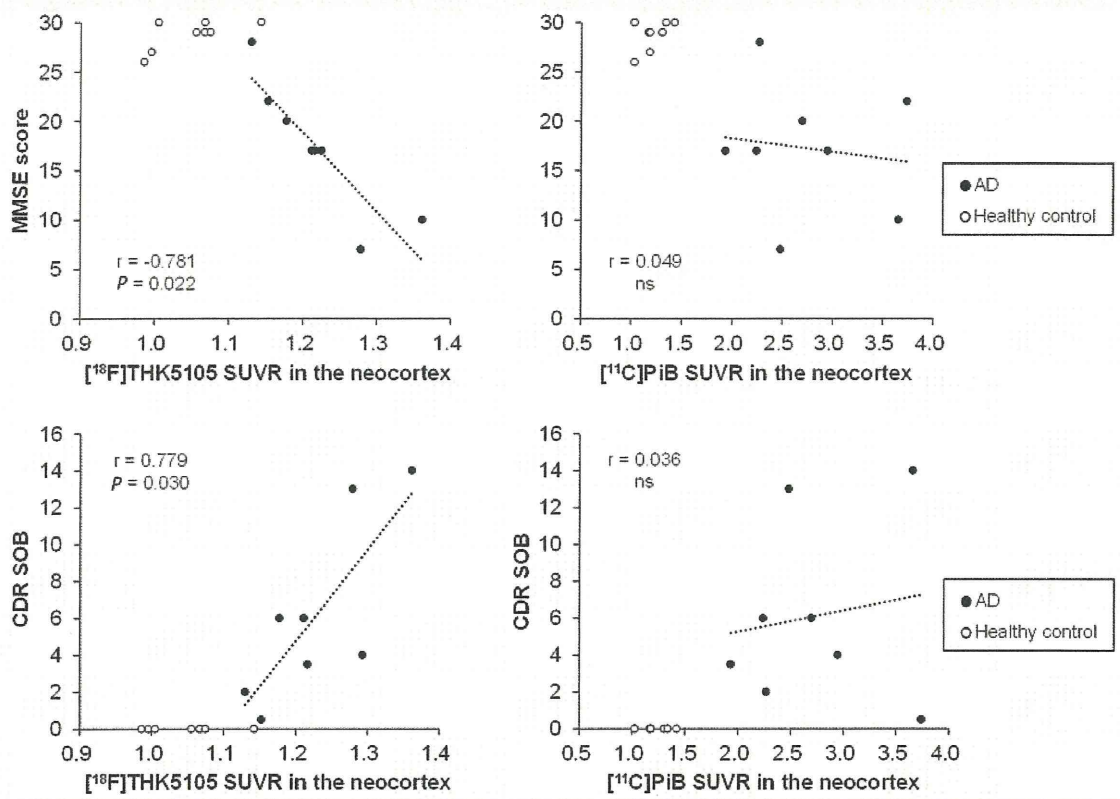


**Figure 6** Correlation of neocortical $^{18}$F-THK5105 and $^{11}$C-PiB SUVR with MMSE scores (*upper*) and CDR-SOB scores (*lower*). Data from eight healthy control subjects (open circles) and eight patients with Alzheimer's disease (AD, filled circles) are shown.

of tau pathology (Soto, 2012; Mohamed *et al.*, 2013) from temporal areas to the other association cortices. A longitudinal assessment of tau pathology will help elucidate the spatial patterns of tau pathology progression in the living brain. In addition, as observed in $^{18}$F-T807 and $^{18}$F-T808 PET studies (Chien *et al.*, 2013, 2014), $^{18}$F-THK5105 retention in the mesial temporal area was relatively lower than in the lateral temporal area in patients with Alzheimer's disease, which conflicts with microscopic observations showing higher neurofibrillary tangle density in the entorhinal cortex and hippocampus of Alzheimer's disease brain compared to the neocortex (Arnold *et al.*, 1991). One possible explanation for this phenomenon is the partial volume effect of radiotracer signals (Muller-Gartner *et al.*, 1992). $^{18}$F-THK5105 retention in the mesial temporal cortex might be underestimated in patients with severe hippocampal atrophy.

$^{18}$F-THK5105 retention in patients with Alzheimer's disease was closely associated with dementia severity. This finding is consistent with results from previous post-mortem studies showing significant correlations of neurofibrillary tangle density with dementia severity (Arriagada *et al.*, 1992; Bierer *et al.*, 1995; Berg *et al.*, 1998). Our results further demonstrate that hippocampal atrophy is significantly correlated with $^{18}$F-THK5105 retention but not with $^{11}$C-PiB retention in the same area. In addition, the neocortical grey matter volume was negatively correlated with global $^{18}$F-THK5105 retention in the neocortex. These findings correspond with the neuropathological observation that the density of neurofibrillary tangles, but not senile plaques, is closely associated with neuronal loss (Gomez-Isla *et al.*, 1996, 1997). Intriguingly, $^{18}$F-THK5105 retention in healthy control subjects was significantly higher in the mesial temporal cortex (SUVR = 1.17) than in the neocortex (SUVR = 1.05). This finding is likely to reflect age-related tau accumulation in this area. In future studies, the association of mesial temporal $^{18}$F-THK5105 retention with ageing should be evaluated in a large population. It is also still unclear whether or not tau accumulation precedes neuronal loss. To answer this question, mesial temporal cortex tau density should be evaluated in the mild cognitive impairment population, as well as cognitively normal individuals with amyloid-β deposition, and these results should be compared with fluorodeoxyglucose and brain atrophy in a longitudinal analysis.

The amount of neocortical $^{18}$F-THK5105 retention (SUVR = 1.23) was considerably lower than that of $^{11}$C-PiB (SUVR = 2.75) in patients with Alzheimer's disease. This is thought to result from higher concentrations of amyloid-β fibrils than tau fibrils in the Alzheimer's disease brain (Villemagne *et al.*, 2012). Therefore, a tau-specific radiotracer must be highly sensitive and selective to tau protein fibrils. Our previous study demonstrated that the binding affinity of $^{18}$F-THK5105 for tau fibrils (Kd = 1.45 nM) was 25-times higher than to amyloid-β fibrils (Kd = 35.9 nM) (Okamura *et al.*, 2013). Autoradiography studies

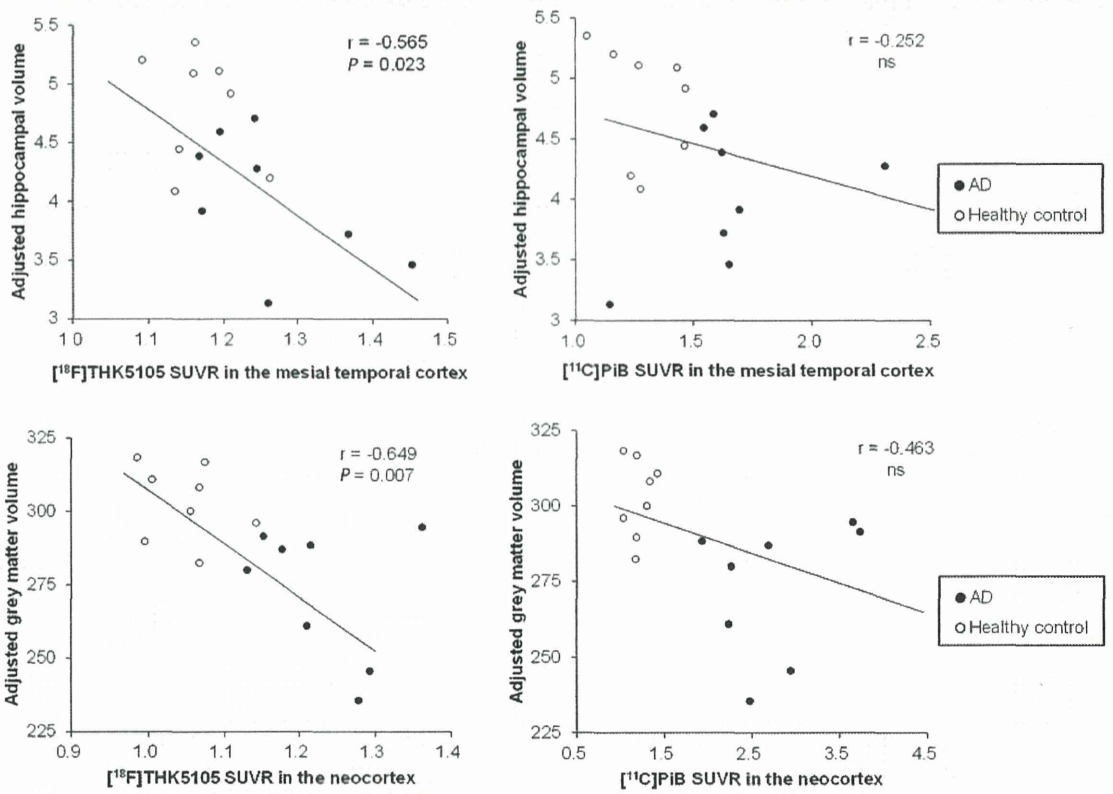


**Figure 7** Correlation of $^{18}$F-THK5105 and $^{11}$C-PiB SUVR with adjusted hippocampal volumes (*upper*) or grey matter volumes (*lower*). Data from eight healthy control subjects (open circles) and eight patients with Alzheimer's disease (AD, filled circles) are shown.

further confirmed the preferential binding ability of $^{18}$F-THK5105 to tau protein deposits in Alzheimer's disease brain sections. In this PET study, all Alzheimer's disease cases were PiB-positive and showed remarkable PiB retention in broad neocortical areas. As reported by many researchers, these patients with Alzheimer's disease showed prominent PiB retention in the ventrolateral prefrontal cortex (SUVR > 2.0), reflecting high amyloid-β pathology in this area. In contrast, $^{18}$F-THK5105 retention in the frontal cortex was not elevated in more than half of the Alzheimer's disease cases (Fig. 4). In addition, one healthy control case showing PiB retention in the frontal cortex showed no retention of $^{18}$F-THK5105 in this area. These results support the low sensitivity of $^{18}$F-THK5105 to amyloid-β plaques.

Compared with previous $^{18}$F-THK523 PET data, specific $^{18}$F-THK5105 retention in grey matter was considerably higher whereas white matter retention was considerably lower than those observed for $^{18}$F-THK523. This observation is consistent with previous *in vitro* autoradiograms showing a higher signal-to-background ratio of $^{18}$F-THK5105 than $^{18}$F-THK523 in Alzheimer's disease brain sections (Okamura *et al.*, 2013). This is probably due to the higher binding affinity of $^{18}$F-THK5105 to tau protein fibrils. The peak brain entry of $^{18}$F-THK5105 (cerebellar SUV = 4.5), which was observed before 6 min post-injection, was higher than for $^{18}$F-THK523 and other reported radiotracers ($^{18}$F-T807, $^{18}$F-T808 and $^{11}$C-PBB3) and almost identical to the reported SUV value of $^{11}$C-PiB (Klunk *et al.*, 2004). In addition, $^{18}$F-THK5105 did not accumulate in the skull, which is often the result of defluorination and interferes with visual PET image inspection. These pharmacokinetic properties are unique advantages of $^{18}$F-THK5105 over the other reported radiotracers. Conversely, one of the drawbacks of $^{18}$F-THK5105 is the existence of non-specific tracer retention in the brainstem, thalamus, and subcortical white matter, which reflects the binding of tracer to β-sheet structures present in myelin basic protein, similar to that observed for $^{11}$C-PiB (Stankoff *et al.*, 2011). Nevertheless, the $^{18}$F-THK5105 signal in the subcortical white matter was not visually noticeable as compared with $^{18}$F-THK523 and $^{11}$C-PiB. The relatively slower kinetics of $^{18}$F-THK5105 cause the high background signals in grey matter, which may make the white matter signals less noticeable. Actually, the clearance of $^{18}$F-THK5105 from normal grey matter tissue was slower than that of PiB because of higher lipophilicity for $^{18}$F-THK5105 (LogP = 3.03) than PiB (LogP = 1.20). As another tau-imaging radiotracer candidate, we have developed a 2-arylquinoline derivative named $^{18}$F-THK5117 (Okamura *et al.*, 2013), which is more hydrophilic and shows faster pharmacokinetics in mice than $^{18}$F-THK5105. It is expected to show faster clearance from normal brain tissue in humans and higher signal-to-background ratio than $^{18}$F-THK5105. A clinical trial testing $^{18}$F-THK5117 is currently underway.

Tau deposits are also present in non-Alzheimer's disease tauopathies including frontotemporal lobe degeneration, corticobasal degeneration, progressive supranuclear palsy and chronic traumatic encephalopathy. Although THK523 failed to detect tau deposits in these non-Alzheimer's disease tauopathies, we recently observed *in vitro* binding ability of THK5105 and THK5117 to glial tau pathology in corticobasal degeneration and progressive supranuclear palsy. Therefore, clinical PET study in non-Alzheimer's disease tauopathies will be necessary to decide whether $^{18}$F-THK5105 is applicable to the study of a broad range of tauopathies.

The results of the current study indicate that $^{18}$F-THK5105 has adequate safety to be used as a clinical PET tracer. $^{18}$F-THK5105 PET demonstrated high tracer retention in sites susceptible to paired helical filament-tau deposition in patients with Alzheimer's disease and distinctly differentiated patients with Alzheimer's disease from age-matched healthy controls. Collectively, these findings suggest that $^{18}$F-THK5105 is useful for the non-invasive evaluation of tau pathology in humans and could be employed to study longitudinal tau deposition in healthy and pathological ageing.

## Acknowledgements

We thank Prof. Michael Woodward, Dr John Merory, Dr Gordon Chan, Dr Kenneth Young, Dr David Darby, Ms Fiona Lamb, and the Brain Research Institute for their assistance with this study.

## Funding

This study was supported by the research fund from GE Healthcare, the SEI (Sumitomo Electric Industries, Ltd) Group CSR Foundation, NHMRC grant 1044361 and NIRG grant from the Alzheimer's Association, the Industrial Technology Research Grant Program of the New Energy and Industrial Technology Development Organization (NEDO) in Japan (09E51025a), Health and Labor Sciences Research Grants from the Ministry of Health, Labor, and Welfare of Japan, Grant-in-Aid for Scientific Research (B) (23390297) and "Japan Advanced Molecular Imaging Program (J-AMP)" of the Ministry of Education, Culture, Sports, Science and Technology (MEXT), Japan.

## References

Abner EL, Kryscio RJ, Schmitt FA, Santacruz KS, Jicha GA, Lin Y, et al. "End-stage" neurofibrillary tangle pathology in preclinical Alzheimer's disease: fact or fiction? J Alzheimers Dis 2011; 25: 445–53.

Arnold SE, Hyman BT, Flory J, Damasio AR, Van Hoesen GW. The topographical and neuroanatomical distribution of neurofibrillary tangles and neuritic plaques in the cerebral cortex of patients with Alzheimer's disease. Cereb Cortex 1991; 1: 103–16.

Arriagada PV, Growdon JH, Hedley-Whyte ET, Hyman BT. Neurofibrillary tangles but not senile plaques parallel duration and severity of Alzheimer's disease. Neurology 1992; 42: 631–9.

Berg L, McKeel DW Jr, Miller JP, Baty J, Morris JC. Neuropathological indexes of Alzheimer's disease in demented and nondemented persons aged 80 years and older. Arch Neurol 1993; 50: 349–58.

Berg L, McKeel DW Jr, Miller JP, Storandt M, Rubin EH, Morris JC, et al. Clinicopathologic studies in cognitively healthy aging and Alzheimer's disease: relation of histologic markers to dementia severity, age, sex, and apolipoprotein E genotype. Arch Neurol 1998; 55: 326–35.

Bierer LM, Hof PR, Purohit DP, Carlin L, Schmeidler J, Davis KL, et al. Neocortical neurofibrillary tangles correlate with dementia severity in Alzheimer's disease. Arch Neurol 1995; 52: 81–8.

Bouras C, Hof PR, Giannakopoulos P, Michel JP, Morrison JH. Regional distribution of neurofibrillary tangles and senile plaques in the cerebral cortex of elderly patients: a quantitative evaluation of a one-year autopsy population from a geriatric hospital. Cereb Cortex 1994; 4: 138–50.

Braak H, Braak E. Neuropathological stageing of Alzheimer-related changes. Acta Neuropathol 1991; 82: 239–59.

Checn DT, Bahri S, Szardenings AK, Walsh JC, Mu F, Su MY, et al. Early *clinical PET imaging results with the novel PHF-tau radioligand* [F-18]-T807. J Alzheimers Dis 2013; 34: 457–68.

Chien DT, Szardenings AK, Bahri S, Walsh JC, Mu FR, Xia CF, et al. Early Clinical PET Imaging Results with the Novel PHF-Tau Radioligand [F18]-T808. J Alzheimers Dis 2014; 38: 171–84.

Fodero-Tavoletti MT, Okamura N, Furumoto S, Mulligan RS, Connor AR, McLean CA, et al. 18F-THK523: a novel *in vivo* tau imaging ligand for Alzheimer's disease. Brain 2011; 134: 1089–100.

Gomez-Isla T, Hollister R, West H, Mui S, Growdon JH, Petersen RC, et al. Neuronal loss correlates with but exceeds neurofibrillary tangles in Alzheimer's disease. Ann Neurol 1997; 41: 17–24.

Gomez-Isla T, Price JL, McKeel DW Jr, Morris JC, Growdon JH, Hyman BT. Profound loss of layer II entorhinal cortex neurons occurs in very mild Alzheimer's disease. J Neurosci 1996; 16: 4491–500.

Grundke-Iqbal I, Iqbal K, Quinlan M, Tung YC, Zaidi MS, Wisniewski HM. Microtubule-associated protein tau. A component of Alzheimer paired helical filaments. J Biol Chem 1986a; 261: 6084–9.

Grundke-Iqbal I, Iqbal K, Tung YC, Quinlan M, Wisniewski HM, Binder LI. Abnormal phosphorylation of the microtubule-associated protein tau (tau) in Alzheimer cytoskeletal pathology. Proc Natl Acad Sci USA 1986b; 83: 4913–7.

Harada R, Okamura N, Furumoto S, Tago T, Maruyama M, Higuchi M, et al. Comparison of the binding characteristics of [$^{18}$F]THK-523 and other amyloid imaging tracers to Alzheimer's disease pathology. Eur J Nucl Med Mol Imaging 2013; 40: 125–32.

Harada R, Okamura N, Furumoto S, Yoshikawa T, Arai H, Yanai K, et al. Use of a benzimidazole derivative BF-188 in fluorescence multispectral imaging for selective visualization of tau protein fibrils in the Alzheimer's disease brain. Mol Imaging Biol 2014; 16: 19–27.

Haroutunian V, Purohit DP, Perl DP, Marin D, Khan K, Lantz M, et al. Neurofibrillary tangles in nondemented elderly subjects and mild Alzheimer disease. Arch Neurol 1999; 56: 713–8.

Klunk WE, Engler H, Nordberg A, Wang Y, Blomqvist G, Holt DP, et al. Imaging brain amyloid in Alzheimer's disease with Pittsburgh Compound-B. Ann Neurol 2004; 55: 306–19.

Lee VM, Balin BJ, Otvos L Jr, Trojanowski JQ. A68: a major subunit of paired helical filaments and derivatized forms of normal Tau. Science 1991; 251: 675–8.

Maruyama M, Shimada H, Suhara T, Shinotoh H, Ji B, Maeda J, et al. Imaging of tau pathology in a tauopathy mouse model and in Alzheimer patients compared to normal controls. Neuron 2013; 79: 1094–108.

Masters CL, Cappai R, Barnham KJ, Villemagne VL. Molecular mechanisms for Alzheimer's disease: implications for neuroimaging and therapeutics. J Neurochem 2006; 97: 1700–25.

Mintun MA, Larossa GN, Sheline YI, Dence CS, Lee SY, Mach RH, et al. [11C]PIB in a nondemented population: potential antecedent marker of Alzheimer disease. Neurology 2006; 67: 446–52.

Mohamed NV, Herrou T, Plouffe V, Piperno N, Leclerc N. Spreading of tau pathology in Alzheimer's disease by cell-to-cell transmission. Eur J Neurosci 2013; 37: 1939–48.

Muller-Gartner HW, Links JM, Prince JL, Bryan RN, McVeigh E, Leal JP, et al. Measurement of radiotracer concentration in brain gray matter using positron emission tomography: MRI-based correction for partial volume effects. J Cereb Blood Flow Metab 1992; 12: 571–83.

Okamura N, Furumoto S, Harada R, Tago T, Yoshikawa T, Fodero-Tavoletti M, et al. Novel 18F-labeled arylquinoline derivatives for non-invasive imaging of tau pathology in Alzheimer disease. J Nucleic Med 2013; 54: 1420–7.

Okamura N, Suemoto T, Furumoto S, Suzuki M, Shimadzu H, Akatsu H, et al. Quinoline and benzimidazole derivatives: candidate probes for *in vivo* imaging of tau pathology in Alzheimer's disease. J Neurosci 2005; 25: 10857–62.

Price JL, McKeel DW Jr, Buckles VD, Roe CM, Xiong C, Grundman M, et al. Neuropathology of nondemented aging: presumptive evidence for preclinical Alzheimer disease. Neurobiol Aging 2009; 30: 1026–36.

Rowe CC, Ng S, Ackermann U, Gong SJ, Pike K, Savage G, et al. Imaging beta-amyloid burden in aging and dementia. Neurology 2007; 68: 1718–25.

Shoghi-Jadid K, Small GW, Agdeppa ED, Kepe V, Ercoli LM, Siddarth P, et al. Localization of neurofibrillary tangles and beta-amyloid plaques in the brains of living patients with Alzheimer disease. Am J Geriatr Psychiatry 2002; 10: 24–35.

Small GW, Kepe V, Ercoli LM, Siddarth P, Bookheimer SY, Miller KJ, et al. PET of brain amyloid and tau in mild cognitive impairment. N Engl J Med 2006; 355: 2652–63.

Soto C. *In vivo* spreading of tau pathology. Neuron 2012; 73: 621–3.

Sperling RA, Aisen PS, Beckett LA, Bennett DA, Craft S, Fagan AM, et al. Toward defining the preclinical stages of Alzheimer's disease: recommendations from the National Institute on Aging-Alzheimer's Association workgroups on diagnostic guidelines for Alzheimer's disease. Alzheimers Dement 2011; 7: 280–92.

Stankoff B, Freeman L, Aigrot MS, Chardain A, Dolle F, Williams A, et al. Imaging central nervous system myelin by positron emission tomography in multiple sclerosis using [methyl-(1)(1)C]-2-(4'-methylaminophenyl)- 6-hydroxybenzothiazole. Ann Neurol 2011; 69: 673–80.

Villemagne VL, Furumoto S, Fodero-Tavoletti MT, Harada R, Mulligan RS, Kudo Y, et al. The challenges of tau imaging. Future Neurol 2012; 7: 409–21.

Villemagne VL, Pike KE, Chetelat G, Ellis KA, Mulligan RS, Bourgeat P, et al. Longitudinal assessment of Abeta and cognition in aging and Alzheimer disease. Ann Neurol 2011; 69: 181–92.

Vos SJ, Xiong C, Visser PJ, Jasielec MS, Hassenstab J, Grant EA, et al. Preclinical Alzheimer's disease and its outcome: a longitudinal cohort study. Lancet Neurol 2013; 12: 957–65.

Research Article

Journal of Labelled Compounds and Radiopharmaceuticals

Received 3 July 2013, Revised 31 August 2013, Accepted 8 September 2013 Published online 16 October 2013 in Wiley Online Library

(wileyonlinelibrary.com) DOI: 10.1002/jlcr.3133

# Synthesis and preliminary evaluation of 2-arylhydroxyquinoline derivatives for tau imaging

Tetsuro Tago,[a] Shozo Furumoto,[a,b]* Nobuyuki Okamura,[b] Ryuichi Harada,[b] Yoichi Ishikawa,[a] Hiroyuki Arai,[c] Kazuhiko Yanai,[b] Ren Iwata,[a] and Yukitsuka Kudo[d]

**Alzheimer's disease (AD) is the most common cause of dementia. Senile plaques, consisting of β-amyloid, and neurofibrillary tangles (NFTs), composed of tau protein, are representative pathological hallmarks of AD. It is believed that the accumulation of NFTs precedes the onset of clinical symptoms of AD and correlates with the progression of memory dysfunction. Thus, the use of noninvasive detection techniques including radiolabeled probes and positron emission tomography (PET) will facilitate early diagnosis or staging of AD. In this study, we synthesized and evaluated novel hydroxylated 2-arylquinoline derivatives as tau imaging PET probes. The binding affinities of compounds for tau were evaluated by fluorescent staining of the AD hippocampal section and a competitive binding assay using [$^{18}$F]THK-523. THK-951 showed high binding affinity for tau pathology in an AD brain section and K18Δ280K fibrils ($K_i$ = 20.7 nM); thus, we radiosynthesized a $^{11}$C-labeled THK-951 and further studied its potential as a tau PET probe. The [$^{11}$C]THK-951 demonstrated excellent kinetics in a normal mouse brain (3.23% ID/g at 2 min postinjection and 0.15% ID/g at 30 min postinjection) and showed the labeling of NFTs in an AD brain section by autoradiography assay. These findings indicate the availability of [$^{11}$C]THK-951 for in vivo PET imaging of tau pathology in AD.**

**Keywords:** Alzheimer's disease; tau; positron emission tomography; imaging

## Introduction

Alzheimer's disease (AD) is a typical neurodegenerative disorder associated with memory impairment, disorientation, and language disorder. Because AD shows complex and diverse clinical symptoms, which overlap with other dementias, its definitive diagnosis is reliant on postmortem examination rather than clinical diagnosis. Neuronal atrophy and deposition of senile plaques (SPs) and neurofibrillary tangles (NFTs) in the brain represent the pathological hallmarks of AD.[1–3] Consequently, noninvasive imaging techniques to measure these pathological changes can be indispensable to the differential diagnosis of AD.

According to amyloid hypothesis, the AD pathogenic mechanism starts with the abnormal accumulation of SPs consisting of β-amyloid aggregation in the brain.[4] With a view to presymptomatic diagnosis, investigation into the detection of lesions using positron emission tomography (PET) or single photon emission computed tomography has been promoted in this decade, and many radiolabeled ligands were developed ([$^{18}$F]FDDNP,[5] [$^{11}$C]PIB,[6] [$^{18}$F]AV-45,[7] [$^{11}$C]BF-227,[8] and [$^{123}$I/$^{125}$I]IMPY[9]).[10] These ligands have been successful for the detection of SPs in living human brains and were useful for confirming the correlation between PET images and autopsy results.[11–13]

Although β-amyloid PET imaging studies have high sensitivity and can detect SPs before clinical symptoms appear, they also showed that the association between Aβ signals and acuteness of symptom was limited.[4,14] Therefore, to estimate AD severity from pathological changes, other quantitatively detectable biomarkers are desired.

Tau proteins, which associate with the stabilization of microtubules, are abnormally phosphorylated and form paired helical filaments (PHFs) in the AD patient's brain.[15,16] PHFs finally assemble into NFTs, neuropil threads, and dystrophic neurites. Neurofibrillary lesions appear in certain brain areas before the onset of dementia, and autopsy studies indicate a higher association between tau pathology levels and cognitive dysfunction relative to Aβ pathology.[17–20] Thus, quantitative imaging of tau burden may serve to not only monitor the progression of neurodegeneration but also evaluate the therapeutic effect of longitudinal tau-targeted AD treatments.

[a]*Cyclotron and Radioisotope Center (CYRIC), Tohoku University, Sendai 980-8578, Japan*

[b]*Department of Pharmacology, Tohoku University School of Medicine, Sendai 980-8575, Japan*

[c]*Department of Geriatrics & Gerontology, Institute of Development, Aging and Cancer, Tohoku University, Sendai 980-8575, Japan*

[d]*Innovation of New Biomedical Engineering Center, Tohoku University, Sendai 980-8574, Japan*

**Correspondence to: Shozo Furumoto, Cyclotron and Radioisotope Center (CYRIC), Tohoku University, 6-3 Aoba, Aramaki, Aoba-ku, Sendai 980-8578, Japan. E-mail: furumoto@cyric.tohoku.ac.jp*

Recently, several tau ligands for PET or single photon emission computed tomography imaging have been reported.[21,22] Kolb and colleagues have reported $^{18}$F-labeled tau tracers, [$^{18}$F]T807 and [$^{18}$F]T808, and these tracers showed promising results in both in vitro and in vivo studies.[23–25] We have developed 2-arylquinoline derivatives with a preference to bind tau lesions rather than A$\beta$ as previously reported.[26,27] Through the structural optimization, we recently reported $^{18}$F-labeled derivatives [$^{18}$F]THK-5105 and [$^{18}$F]THK-5117.[28] They appear to have more preferable properties as a PET tau imaging radiotracer compared with [$^{18}$F]THK-523.[27] The preliminary clinical studies using these tracers are currently in progress.

Lipophilic ligands display higher nonspecific binding; therefore, lower lipophilicity is important for ideal brain kinetics as brain imaging PET tracers. Low nonspecific binding contributes to high signal-to-background ratio and facilitates the visualization of lower burden of tau pathology. The aim of the present study was to develop a $^{11}$C-labeled tau probe with fast clearance from nonspecific regions. We developed novel hydroxylated quinoline derivatives (Figure 1) with lower lipophilicity and evaluated their potential as tau probes for PET.

## Experimental

### Synthesis of 2-arylquinoline derivatives

Methods for the synthesis and characterization data of 2-arylquinoline derivatives (shown in Schemes 1 and 2) are described in detail in the Supporting Information.

### Radiolabeling of [$^{11}$C]THK-951

[$^{11}$C]Methyl iodide was prepared from [$^{11}$C]carbon dioxide produced with a Cypris HM12 cyclotron (Sumitomo Heavy Industries Inc., Tokyo, Japan) by a catalytic iodination reaction via [$^{11}$C]methane (Mel MicroLab, GE Healthcare, Waukesha, WI, USA). [$^{11}$C]Methyl triflate ([$^{11}$C]MeOTf) used for radiolabeling was prepared from [$^{11}$C]methyl iodide by passing through a silver triflate-graphpac (Sigma-Aldrich, St Louis, USA) gas chromatography column heated at 200 °C. The compound **15** indicated in Scheme 2 was used as a radiolabeling precursor. The precursor (1.0 mg) and tBuOK (1.0 mg) were dissolved in dimethyl sulfoxide (DMSO) (400 µL). [$^{11}$C]MeOTf was bubbled through the solution, followed by heating at 110 °C for 1 min. Then, 2 N HCl (1 mL) was added to the solution, and it was heated at an additional 10 min at the same temperature. The solution was neutralized with 4 N NaOH (0.5 mL), and the crude mixture was purified with semi-preparative HPLC using an Inertsil® ODS-3 (GL Sciences Inc., Tokyo, Japan) eluted with acetonitrile/20 mM $NaH_2PO_4$ (pH 4.8) (40/60, flow rate: 5.0 mL/min). The fraction containing [$^{11}$C]THK-951 was mixed with water (20 mL) and 25% ascorbic acid (0.5 mL) and passed through an activated Sep-Pak tC18 Plus (Waters, Milford, MA, USA). The Sep-Pak cartridge was washed with water, and then, [$^{11}$C]THK-951 was eluted with ethanol. The ethanol solution was used for the in vitro autoradiography (ARG) assay. For the ex vivo biodistribution study, ethanol was removed by evaporation, and the product was solubilized into saline with polysorbate 80 (<0.1%).

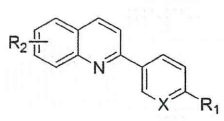


**Figure 1.** Chemical structure of hydroxyquinoline derivatives. Compounds in this study include the following: X = CH, N; $R_1$ = $NH_2$, $NHCH_3$; $R_2$ = 6-OH, 7-OH.

### Measurement of logP values

The octanol/water partition coefficients of the tested compounds were estimated by HPLC method of the OECD (Organisation for Economic Co-operation and Development) guideline[29] according to the slightly modified procedures we recently reported.[28]

### In vitro fluorescent binding assay with tau fibrils

*Preparation of K18Δ280K-tau fibrils*

Recombinant K18Δ280K-tau was custom generated by Life Technologies Japan Ltd. (Tokyo, Japan). K18Δ280K-tau fibrils were prepared as described previously.[27,30] Briefly, K18Δ280K-tau solution was diluted with phosphate buffered saline (pH 7.4) to a final concentration of 20 µM. The solution was incubated at 37 °C for a day with agitation (1000 rpm). Fibril formation was confirmed by thioflavin-S fluorescence spectroscopy.

### In vitro fluorescence binding assay

Synthetic K18Δ280K-tau fibrils (200 nM) were incubated with 3 µM (THK-951 and THK-5272) or 5 µM (THK-953 and THK-5273) compounds at room temperature for 1 h. The fluorescence intensity was measured at an excitation wavelength appropriate for each compound. The incubations were carried out on Nunc 96 MicroWell™ black plates (Nalge Nunc Int., Rochester, NY, USA), using 200 µL of phosphate buffer saline (pH 7.4) as the reaction mixture. All experiments were conducted in triplicate.

### In vitro neuropathological staining using brain sections

The staining properties of the tested compounds were examined using postmortem brain tissues from an autopsy-confirmed case of AD (82-year-old woman). The experiments were performed in accordance with the regulations of the ethics committee of Tohoku University. A series of 8 µm thick sections from paraffin-embedded blocks of hippocampus were used for staining. According to the method reported previously,[28,31] the sections were immunostained with anti-tau antibody (AT8; Innogenetics, Ghent, Belgium). Stained images were examined using an Olympus (Tokyo, Japan) BX51 microscope equipped with blue-violet (BP, 400–440; DM, 455; BA, 475) and blue filters (BP, 460–490; DM, 500; BA, 520IF).

### Competitive binding assay with [$^{18}$F]THK-523

[$^{18}$F]THK-523 was synthesized as described previously.[27] The product was formulated with DMSO. The specific activity of [$^{18}$F]THK-523 was 121.7 GBq/µmol (end of synthesis), and the radiochemical purity was >99%. Competitive binding assay was performed as described previously[28] with [$^{18}$F]THK-523 (final concentration: 4.1 nM) used as a radioligand of the assay.

### Autoradiography of [$^{11}$C]THK-951

The hippocampal brain sections from a case of AD (82-year-old woman) were used for in vitro ARG. Deparaffinized sections were treated with a saline solution of [$^{11}$C]THK-951 (25% ethanol, 0.4 MBq/mL) or [$^{18}$F]THK-523 (25% DMSO, 0.6 MBq/mL) for 10 min at room temperature. The sections were washed briefly with $H_2O$ and 50% ethanol. After drying, the labeled sections were exposed to a BAS-III imaging plate (Fuji Film, Tokyo, Japan) for 3 h ([$^{11}$C]THK-951) or overnight ([$^{18}$F]THK-523). Autoradiographic images were obtained using the BAS-5000 phosphor imaging instrument (Fuji Film). Adjacent brain sections were immunostained with anti-tau antibody (AT8; Innogenetics) and anti-A$\beta$ antibody (6F/3D; Dako, Glostrup, Denmark).

### Ex vivo biodistribution assay of [$^{11}$C]THK-951 in normal mice

Ex vivo biodistribution assay was performed as described previously.[28] Briefly, [$^{11}$C]THK-951 (saline solution: 1.8–1.9 MBq/200 µL) was administered to male ICR mice (average weight: 29 g) via the tail vein. The mice were anesthetized with isoflurane and sacrificed by decapitation at 2, 10, 30, 60, and 90 min postinjection. The brain, blood, and other organs were excised.

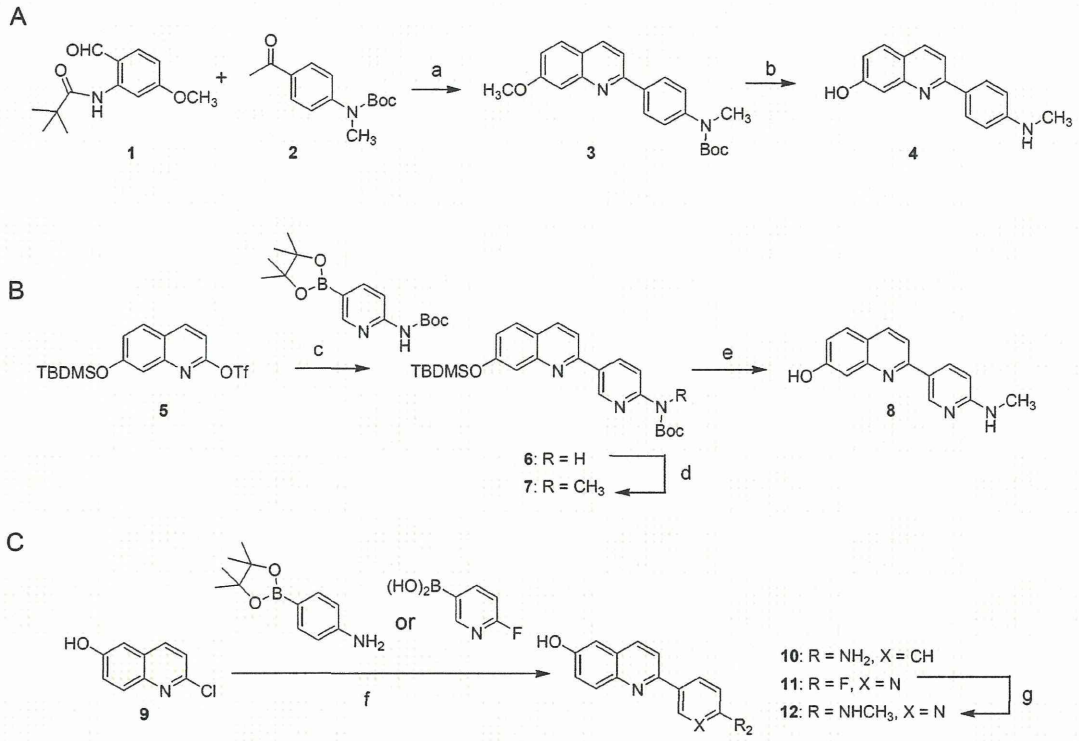


**Scheme 1.** Synthesis of hydroxyquinoline derivatives (refer to Supporting Information). A: Synthesis of THK-951. (a) KHMOS, THF. (b)$BBr_3$, $CH_2Cl_2$. B: Synthesis of THK-953. (c) $Na_2CO_3$, $Pd(PPh_3)_4$, DME/$H_2O$. (d) $CH_3I$, NaH, DMF. (e) 1. TBAF, THF, 2. TFA, $CH_2Cl_2$. C: Synthesis of THK-5272 and THK-5273. (f) $Na_2CO_3$, $Pd(PPh_3)_4$, DME/$H_2O$/EtOH. (g) $NH_2CH_3$, MeOH.

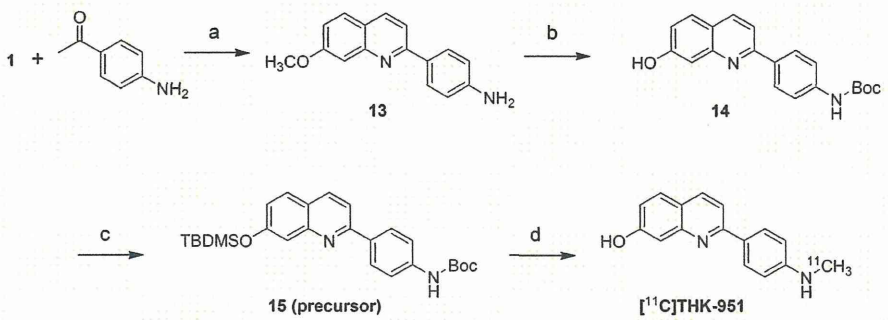


**Scheme 2.** Synthesis of the precursor (refer to Supporting Information) and radiosynthesis of [$^{11}$C]THK-951. (a) 1. KHMOS, THF, 2. concentrated HCl, EtOH. (b) 1. $BBr_3$, $CH_2Cl_2$, 2. $(Boc)_2O$, $NaHCO_3$, THF/$H_2O$, 3. aqueous KOH, MeOH. (c) TBDMSCl, imidazole, DMF. (d) 1. [$^{11}$C]$CH_3OTf$, tBuOK, DMSO, 2. 2 N HCl.

After the organs were weighed, their radioactivity was counted with an automatic $\gamma$-counter. The percentage injected dose per gram (%ID/g) was calculated by comparing tissue counts to tissue weight. Each % ID/g value is an average of four separate experiments.

## Results and discussion

Pittsburgh compound B, a representative $\beta$-amyloid probe for PET, is a 6-hydroxy substituted derivative of 2-arylbenzothiazole. Introduction of a hydroxyl group resulted in low lipophilicity of the probe and rapid clearance of free radioactivity from the brain.[6] These characteristics are essential features for brain imaging probes because nonspecific signals interfere with quantitative analysis of PET images. Therefore, we focused on hydroxyl substituted BF-158 derivatives as tau imaging probe candidates expecting they would provide appropriate brain kinetics.

The synthetic procedures of THK-951, THK-953, THK-5272, and THK-5273 are shown in Scheme 1 (details of the synthesis are described in the Supporting Information). THK-951 is a 2-pheny lquinolin-7-ol derivative synthesized through a condensation reaction of two phenyl rings (Scheme 1A). The cyclocondensation of benzaldehyde (**1**) and acetophenone (**2**) in the presence of potassium *bis*(trimethylsilyl)amide gave **3**. THK-951 (**4**) was obtained by the deprotection of **3** by boron tribromide.

The THK-953 synthesis was outlined in Scheme 1B. **6** was obtained by Suzuki coupling between 7-hydroxyl-protected quinoline triflate (**5**) and pyridine boronic acid pinacol ester. After the *N*-methylation (**7**), deprotection of the TBDMS and Boc groups by treating with TBAF and TFA, respectively, gave THK-953 (**8**).